Available online at www.sciencedirect.com
SCIENCE DIRECT®
Journal of Magnetic Resonance 169 (2004) 102–117
JMR Journal of Magnetic Resonance
www.elsevier.com/locate/jmr

Centric scan SPRITE magnetic resonance imaging: optimization of SNR, resolution, and relaxation time mapping

M. Halse,[a] J. Rioux,[a] S. Romanzetti,[b] J. Kaffanke,[b] B. MacMillan,[a] I. Mastikhin,[a] N.J. Shah,[b] E. Aubanel,[c] and B.J. Balcom[a,*]

[a] *MRI Centre, Department of Physics, University of New Brunswick, Fredericton, NB, Canada*
[b] *MR Group, IME Forschungszentrum Juelich, Germany*
[c] *Faculty of Computer Science, University of New Brunswick, Fredericton, NB, Canada*

Received 21 January 2004; revised 5 April 2004
Available online 10 May 2004

Abstract

Two strategies for the optimization of centric scan SPRITE (single point ramped imaging with T_1 enhancement) magnetic resonance imaging techniques are presented. Point spread functions (PSF) for the centric scan SPRITE methodologies are numerically simulated, and the blurring manifested in a centric scan SPRITE image through PSF convolution is characterized. Optimal choices of imaging parameters and k-space sampling scheme are predicted to obtain maximum signal-to-noise ratio (SNR) while maintaining acceptable image resolution. The point spread function simulation predictions are verified experimentally. The acquisition of multiple FID points following each RF excitation is described and the use of the Chirp z-Transform algorithm for the scaling of field of view (FOV) of the reconstructed images is illustrated. Effective recombination of the rescaled images for SNR improvement and T_2^* mapping is demonstrated.

Keywords: Conical-SPRITE; Spiral-SPRITE; Chirp z-Transform; T_2^* mapping; Point spread function; MRI

1. Introduction

Single point imaging (SPI), also known as constant time imaging, MRI techniques have been demonstrated to be ideal for imaging short relaxation time systems [1–4]. SPI is a pure phase encode technique and therefore images acquired using SPI methods are free from artifacts arising from B_0 inhomogeneity, susceptibility variations, and chemical shift [5]. SPI techniques encode k-space through repetitive broadband RF pulses applied in the presence of variable amplitude phase encode gradients. A single k-space datum point is acquired at an encoding time, t_p, following each RF excitation. SPI methods suffer from long acquisition times because increased acquisition speeds necessitate rapid gradient switching, leading to excessive gradient vibration due to impulsive Lorentz forces. The single point ramped imaging with T_1 enhancement (SPRITE) MRI technique [6] utilizes the SPI method of acquisition in conjunction with a linearly ramped primary phase encode gradient. This methodology greatly reduces the gradient switching requirements and thus allows for more rapid image acquisition without excessive gradient vibration [6].

SPRITE acquisition times and duty cycles have been significantly reduced and sensitivity increased in the Spiral-SPRITE and Conical-SPRITE methodologies through the implementation of centric order k-space sampling schemes [7]. Nonetheless the underlying single point acquisition methodology dictates that even these more rapid SPRITE sampling methods are inefficient compared to frequency encode methods where entire lines in k-space are acquired following each excitation of the spin system. Consequently, the highest quality and most sensitive Spiral-SPRITE and Conical-SPRITE experiments must make efficient use of all available information through the sampling of multiple FID points, and use optimal k-space sampling schemes and imaging

* Corresponding author. Fax: +1-506-453-4581.
E-mail address: bjb@unb.ca (B.J. Balcom).

1090-7807/$ - see front matter © 2004 Elsevier Inc. All rights reserved.
doi:10.1016/j.jmr.2004.04.008

parameters. In this work the collection of multiple FID points following each RF excitation is proposed for the purposes of T_2^* mapping and signal averaging for SNR improvement. In Halse et al. [7], numerically simulated point spread functions were presented for Spiral-SPRITE and Conical-SPRITE experiments. Here, further investigation of the features of these point spread functions, and their blurring effects, have been undertaken. Numerical simulations and imaging experiments have been used to determine the optimal choice of k-space sampling scheme and imaging parameters for maximum signal with an acceptable image resolution.

2. Theory

2.1. Multiple FID point acquisitions

Single point imaging experiments are considered inefficient in comparison to frequency encoding methods because only a single datum point is acquired following each RF excitation. It is sensible to increase the efficiency of SPI methods by collecting multiple FID points following each RF pulse. On many scanners it is impossible to acquire only a single datum point. In these cases, the additional FID points automatically acquired by the scanner are discarded. This is clearly unproductive and a lost opportunity. These additional FID points can be used for signal averaging to improve SNR and/or to accomplish T_2^* mapping.

Fig. 1A depicts the pulse sequence diagram for Spiral-SPRITE with a multiple FID point acquisition. This pulse sequence employs a modified Archimedean spiral trajectory and can be employed with any number of spiral interleaves. Fig. 1B shows a schematic k-space trajectory with a single spiral interleaf while Fig. 1C shows an analogous four spiral interleaves case.

The signal associated with a single datum point acquired at an encoding time, t_p, in the presence of constant phase encode gradient, $\mathbf{G_x}$, is given by

$$S(k_x) = \int \rho_{\text{app}} \sin\alpha e^{t_p/T_2^*} e^{-i2\pi k_x \cdot x}\, dx, \tag{1}$$

where

$$k_x = \frac{1}{2\pi}\gamma G_x t_p, \tag{2}$$

α is the flip angle, γ is the gyromagnetic ratio, and ρ_{app} is the apparent nuclei density, including all sampling and longitudinal magnetization relaxation effects. Each FID point collected following the RF excitation pulse is acquired with a unique encoding time, $t_p + (n-1)\Delta t_p$, where t_p is the initial encoding time, Δt_p is the time between FID points, and n is the index of the given FID point. From Eqs. (1) and (2) it is apparent that the difference in t_p values between FID points will affect both the T_2^* weighting of each point and also the k-space

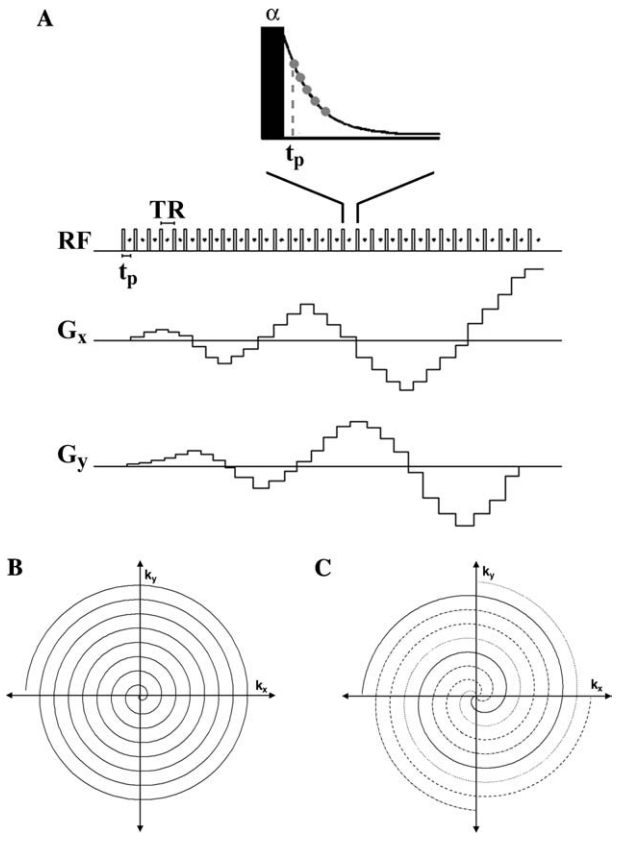

Fig. 1. (A) The Spiral-SPRITE pulse sequence with multiple FID point acquisitions following each RF excitation. Multiple FID points are acquired after an initial encoding time, t_p, separated in time by a fixed dwell time, Δt_p. The k-space trajectory can be altered, to include spiral interleaves for example, by changing the gradient waveforms. (B) A schematic of a single spiral interleaf trajectory. (C) A schematic of a spiral trajectory with four interleaves.

encoding. The T_2^* weighting can be used to advantage in T_2^* mapping applications, or minimized through the use of short dwell times in the case of signal averaging. The different k-space encodings for each FID point is a feature which must be explored and corrected before general use of these data points can be envisioned.

Consider a SPRITE experiment with multiple FID points acquired after each RF excitation. Within this single experiment, an entire set of k-space data points is acquired for each t_p value. Each of these data sets, with a k-space step size unique to the particular t_p, can be reconstructed into a complete image. The FOV of any one of these images is inversely proportional to the k-space step size, Δk, and thus to t_p

$$\text{FOV} = \frac{1}{\Delta k} = \frac{2\pi}{\gamma \Delta G t_p}. \tag{3}$$

The result of a SPRITE experiment, with a multiple FID point acquisition, is a set of complete images, each weighted by the T_2^* decay and each with slightly different fields of view. Prior to image recombination for T_2^* mapping or signal averaging, all images much be

corrected to a common field of view. As proposed by Heid [8] in an ISMRM abstract, a Chirp z-Transform algorithm can be implemented to scale the fields of view.

2.2. FOV scaling using the Chirp z-Transform

In general, the z-Transform of the set of numbers, x_n, can be defined by

$$X(z_k) = \sum_{n=0}^{N-1} x_n z_k^{-n}, \tag{4}$$

where there exist N non-zero points in the sequence of numbers, x_n. The Chirp z-Transform (CZT) algorithm of Rabiner et al. [9] can be used to evaluate the z-Transform on any spiral or circular contour in the z-plane. This contour in the z-plane is defined by

$$z_k = AW^{-k}.$$

The CZT algorithm can be applied to the unit circle contour in the z-plane (Eq. (5))

$$A = \mathrm{e}^{\mathrm{i}\theta_0}; \quad W = \mathrm{e}^{\mathrm{i}\phi_0},$$

$$X(z_k) = \sum_{n=0}^{N-1} x_n \mathrm{e}^{-\mathrm{i}n\theta_0} \mathrm{e}^{\mathrm{i}nk\phi_0}. \tag{5}$$

The parameters, θ_0 and ϕ_0, are the initial angle of the z-plane trajectory and the angular step, respectively. If evaluated over a single rotation of the unit circle, as demonstrated in Eq. (6), the Chirp z-Transform is the discrete Fourier transform

$$\theta_0 = 0; \quad \phi_0 = -\frac{2\pi}{N},$$

$$X(z_k) = \sum_{n=0}^{N-1} x_n \mathrm{e}^{-\mathrm{i}2\pi nk/N}. \tag{6}$$

Hence, the CZT evaluated on the unit circle can be used to transform between k-space and image space.

Through careful choices of θ_0 and ϕ_0, the CZT can be used to simultaneously transform from k-space to image space and scale the image FOV. First, we define a field of view scaling factor, Z, as the ratio between the desired field of view of the image, $\mathrm{FOV}_{\mathrm{des}}$, to the actual field of view of the image, $\mathrm{FOV}_{\mathrm{act}}$, in terms of their respective t_{p} values (Eq. (7))

$$Z = \frac{\mathrm{FOV}_{\mathrm{des}}}{\mathrm{FOV}_{\mathrm{act}}} = \frac{t_{\mathrm{p_{act}}}}{t_{\mathrm{p_{des}}}}. \tag{7}$$

Consider the 1D case depicted in Fig. 2. The actual image includes the spatial positions from 0 to $\mathrm{FOV}_{\mathrm{act}}$, which we normalize to unity for simplicity. This range of spatial positions can be associated with the angles from 0 to 2π. The Chirp z-Transform, when evaluated along the entire unit circle, i.e., over the range of angles from 0 to 2π, is simply the discrete Fourier transform and therefore yields an image with $\mathrm{FOV} = \mathrm{FOV}_{\mathrm{act}}$. To transform the k-space data into image space such that the resultant image has $\mathrm{FOV} = Z * \mathrm{FOV}_{\mathrm{act}} = \mathrm{FOV}_{\mathrm{des}}$, the Chirp z-Transform is evaluated over the range of angles corresponding to $1/2(1-Z)$ through $1/2(1+Z)$, i.e., the CZT is evaluated in N steps, with an initial angle and an angular step of

$$\theta_0 = \pi(1-Z); \quad \phi_0 = 2\pi\frac{Z}{N}.$$

Most practical applications for this image scaling method require the total image intensity to remain invariant over the FOV correction. Through the scaling of the image FOV the physical dimensions of the sample represented by each voxel are altered by a factor of Z^n, where n denotes the number of dimensions scaled. For the total signal to remain invariant over this transformation a correction by Z^n must be applied to the signal in each voxel of the scaled image. However, while maintaining the invariance of the absolute image intensity, this correction introduces an inconsistency into the SNR of the FOV-corrected multiple FID point images. The correction factor is applied to both the signal and to the noise. Therefore, the SNR of the FOV-corrected image remains the same as the SNR of the uncorrected image. This means that each successive multiple FID point image will have different SNR values. This effect is minimal if the extent of FOV zooming is small. We typically limit Z to values greater than 0.8.

2.3. Signal averaging of multiple FID point images

The number of multiple FID point images which can be sensibly signal averaged to yield the maximum SNR advantage is constrained by two conditions. The time between multiple FID point acquisitions, Δt_{p}, must be sufficiently large to avoid noise correlation in images reconstructed from successive FID points, and the extent of FOV scaling must be limited to maintain an acceptable spatial resolution.

To ensure that the noise between multiple FID point images is uncorrelated, the dwell time between FID points must be greater than the inverse of twice the filter width [10]. For an SPI experiment, in order to accommodate the entire frequency range of the image, the filter width is constrained by

$$\mathrm{FW} \geqslant \frac{n}{4t_{\mathrm{p}}}, \tag{8}$$

where n is the number of points in one dimension and t_{p} is the minimum encoding time [5]. For the optimal filter width value (given by the equality in Eq. (8)), the dwell time between multiple FID point images must comply with Eq. (9) in order to obtain the maximum SNR advantage of signal averaging

$$\Delta t_{\mathrm{p}} \geqslant \frac{2t_{\mathrm{p}}}{n}. \tag{9}$$

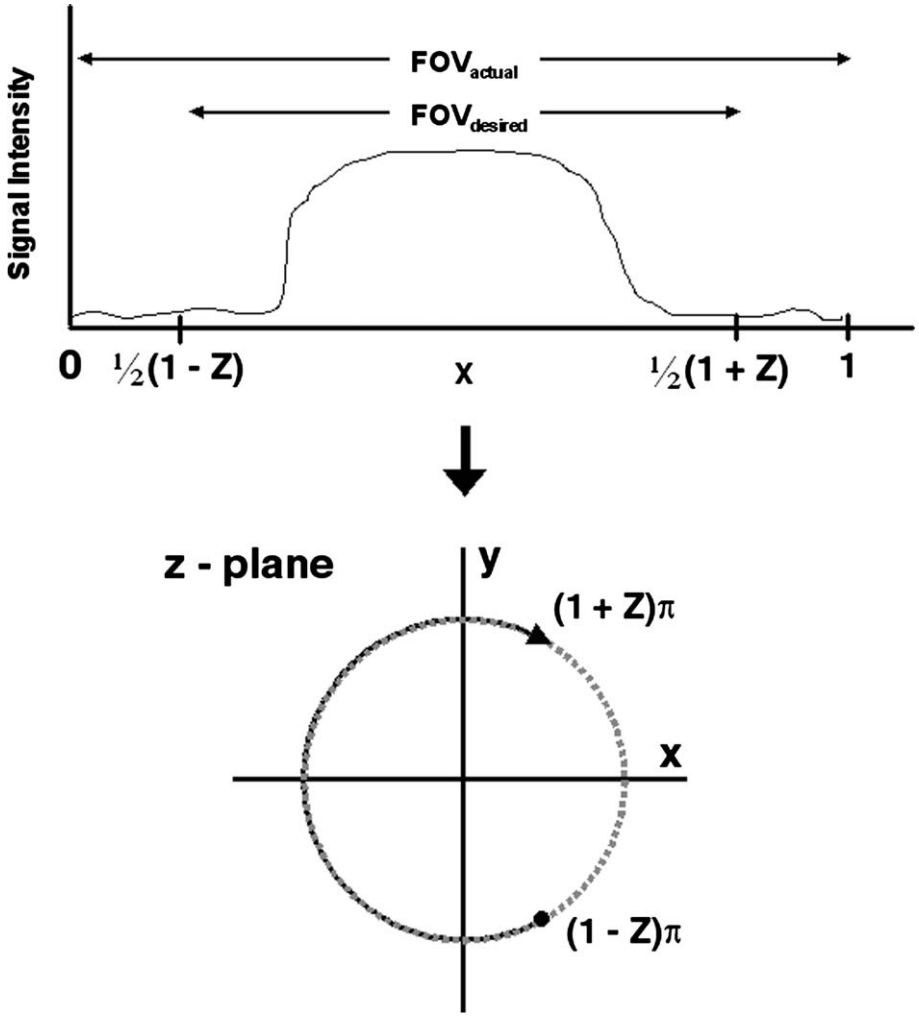

Fig. 2. When evaluated over the entire unit circle in the z-plane, the CZT is the DFT and yields an image with FOV = $\mathrm{FOV}_{\mathrm{actual}}$. The CZT evaluated on the unit circle in the z-plane only over the angles from $(1-Z)\pi$ to $(1+Z)\pi$ (corresponding to the spatial positions $1/2(1-Z)$ to $1/2(1+Z)$) yields an image with $\mathrm{FOV} = Z * \mathrm{FOV}_{\mathrm{actual}} = \mathrm{FOV}_{\mathrm{desired}}$.

The range of encoding times acquired in an experiment with m acquired FID points, at the optimal Δt_{p} (given by the equality in Eq. (9)), with an initial encoding time of t_{p} is

$$\left[t_{\mathrm{p}}, t_{\mathrm{p}} + \frac{2t_{\mathrm{p}}}{n}(m-1)\right]. \tag{10}$$

For a given limit, Z_{lim}, on the extent of FOV scaling, the number of multiple FID point images which can be signal averaged to obtain an increase in SNR is

$$m \leqslant \frac{n}{2}\left(\frac{1}{Z_{\mathrm{lim}}} - 1\right) + 1. \tag{11}$$

For example, in the case of $n = 64$ and $Z_{\mathrm{lim}} = 0.8$ the maximum number of multiple FID data points which can be used to advantage for signal averaging is 9. This relationship limiting the maximum number of multiple FID data points to be used is independent of the initial encoding time. Therefore, a short initial encoding time can be chosen to minimize the signal loss due to the T_2^* decay.

2.4. T_2^* mapping with multiple FID points

The image reconstructed from each FID point is weighted by the T_2^* decay according to the encoding time, t_{p}. These images are scaled to the smallest FOV acquired, that of the longest t_{p} value. Once the images have been corrected to this consistent FOV, a T_2^* decay curve can be defined for each voxel in the image.

The signal equation for a centric scan SPRITE MR image, Eq. (12), indicates that the back-extrapolated intensity obtained from the T_2^* fit is proportional to the nuclei density. Therefore, the multiple FID point fitting procedure yields a T_2^* map and a nuclei density map

$$s = \rho \mathrm{e}^{-t_{\mathrm{p}}/T_2^*} \sin\alpha. \tag{12}$$

The use of multiple FID points for T_2^* mapping will be limited in practice by the extent of FOV scaling required. The spatial resolution of the map is constrained by the spatial resolution of the image acquired at the shortest t_{p}, with the largest FOV and hence the lowest

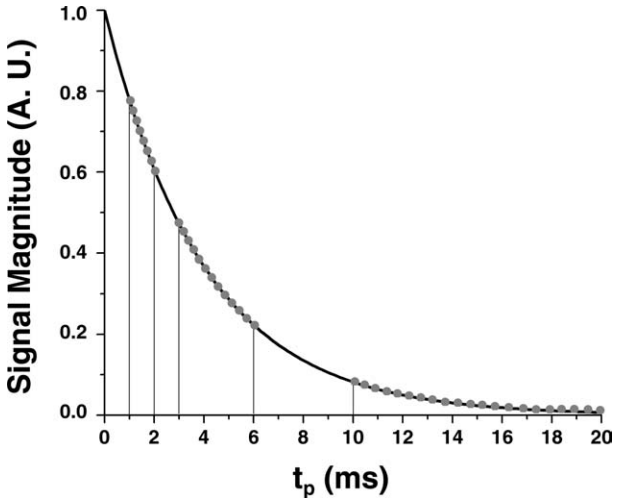

Fig. 3. An illustration of a multiple FID point acquisition scheme for the purpose of T_2^* mapping. The range of t_p values acquired in a single experiment is confined to a factor of two. The t_p ranges from 1 to 2 ms, 3 to 6 ms, and 10 to 20 ms are acquired in separate experiments. In each of these experiments, the gradient step size is set such that the FOV of the last image in each cluster of multiple points (i.e., the images reconstructed from the points acquired at t_p values of 2.0, 6.0, and 20.0 ms) has the desired FOV. The FOV of each multiple point image is scaled to the FOV of the last multiple point image acquired in the same experiment. Therefore, in the scheme depicted in this figure, $Z \geqslant 0.5$.

spatial resolution. To obtain maps with acceptable spatial resolution it is necessary to limit the extent of FOV rescaling of multiple FID point images within a single experiment. This in turn limits the range of t_p values which can be used from a single acquisition.

The range of t_p values required to accurately define a T_2^* decay curve will be much greater than the acceptable t_p range for a single experiment. Therefore, the entire decay curve must be acquired in several separate experiments. In each individual experiment a cluster of FID points covering an acceptable range of t_p values are acquired with a gradient step value set such that the FOV of the image reconstructed from the FID point acquired at the longest t_p is equal to the desired FOV. The multiple FID point images acquired within a single experiment are scaled to the FOV of the longest t_p within that experiment. These sets of rescaled images can then be combined such that a T_2^* decay curve, defined by clusters of t_p points, can be reconstructed for each voxel in the image (Fig. 3). Through the exponential fitting of each of these T_2^* decay curves, a T_2^* map with an acceptable spatial resolution can be obtained.

2.5. Imaging parameter optimization using PSF simulations

The Fourier relationship between the k-space signal, $S(k_x)$, and the resultant image in real space, $s(x)$, for a centric scan SPRITE experiment is given by Eqs. (13) and (14), where $M(k_x)$ is the excited signal, including all transverse magnetization decay effects, $U(t)$ is the k-space sampling function, $R(t)$ is the longitudinal magnetization evolution function, the ideal image, $m(x)$, is the Fourier transform of $M(k_x)$ and the point spread function, PSF, is the Fourier transform of $U(t) * R(t)$

$$S(k_x) = M(k_x)U(t)R(t) \tag{13}$$

Fourier $\updownarrow$ Relationship

$$s(x) = m(x) \otimes \mathrm{PSF}. \tag{14}$$

Eq. (14) dictates that the actual image resolution is the ideal image resolution degraded by a convolution with the PSF. This suggests that the investigation of simulated point spread functions can provide a means of predicting the effect on actual image resolution of k-space sampling schemes and imaging parameters.

The longitudinal magnetization evolution function for an SPI experiment is an effective exponential decay describing the progression from the equilibrium longitudinal magnetization to a steady state. Using the notation of Mastikhin et al. [11], the available longitudinal magnetization after n RF pulses, without magnetization preparation, is

$$M_{z,n}(\mathrm{TR}) = M_0(1-w)\mathrm{e}^{-n\mathrm{TR}/T_{1\mathrm{app}}} + M_0 w, \tag{15}$$

where

$$w = \frac{1-\mathrm{e}^{-\mathrm{TR}/T_1}}{1-\cos\alpha\mathrm{e}^{-\mathrm{TR}/T_1}}, \tag{16}$$

$$\frac{1}{T_{1\mathrm{app}}} = \frac{1}{T_1} - \frac{\ln(\cos\alpha)}{\mathrm{TR}}, \tag{17}$$

where TR is the time period between successive RF excitation pulses, α is the flip angle, and M_0 is the equilibrium longitudinal magnetization. This evolution function, as depicted in Fig. 4, can be considered as the sum of two components: a transient $T_{1\mathrm{app}}$ exponential decay function, and a steady-state function, $M_0 w$. The relative significance of these two functions is determined by the steady-state quantity, w, given by Eq. (16).

Fig. 5A depicts the product of longitudinal magnetization evolution function with the Spiral-SPRITE single spiral sampling function, $R(t) * U(t)$. The Fourier transform of this function is the point spread function (Fig. 5B). The numerically simulated point spread function is a Lorentzian-like peak with FWHM = 1.6 pixels. The product function in Fig. 5A can be separated into a transient and a steady-state function. The steady-state function (Fig. 6A) is simply the sampling function reduced by the constant steady-state value, whereas the transient function (Fig. 6C) is the $T_{1\mathrm{app}}$ decay of the longitudinal magnetization evolution function 'wrapped' around the spiral k-space trajectory.

As a consequence of the linearity property of the Fourier transform, the PSF can be considered as the sum of the Fourier transform of the steady-state function

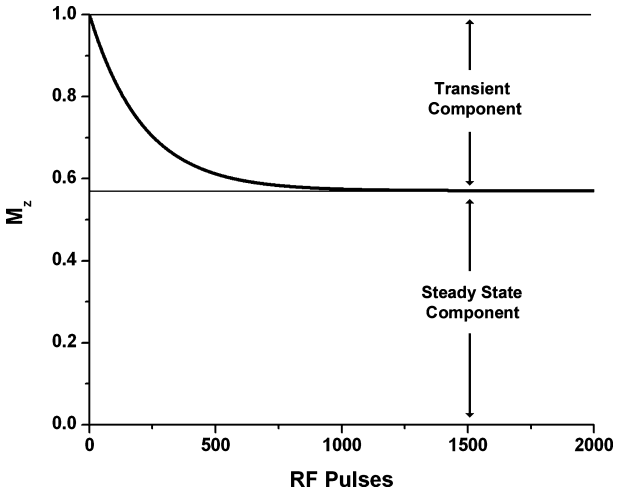

Fig. 4. The longitudinal magnetization evolution function for $TR/T_1 = 2\%$ and $\alpha = 10°$ with the initial magnetization normalized to unity. This function can be separated into the sum of a transient function, the T_{1app} exponential decay (Eq.(17)), and a steady-state function, w (Eq. (16)).

(Fig. 6B) and of the Fourier transform of the transient function (Fig. 6D). The structure of the Fourier transform of the steady-state function, the steady-state point spread function, PSF_{SS}, is determined solely by the sampling function and can be considered to be the sampling point spread function (SPSF) with a total area determined by w, the steady-state fraction. The structure of the Fourier transform of the transient function, the transient point spread function, PSF_{TR}, includes both sampling and longitudinal magnetization evolution effects but is dominated by the evolutionary effects. Therefore, it can be considered to be representative of the evolution point spread function (EPSF), with a total area weighted by $(1 - w)$.

The PSF_{SS} and the PSF_{TR} have Lorentzian-like shapes with low lying structure at the edges of image space due to omitted Cartesian grid points in the k-space trajectory. Convolution with each of these functions will result in a blurring which can be characterized by a full width half maximum (FWHM). The true image resolution will reflect the cumulative effects of convolution with each constituent point spread function: PSF_{SS} and PSF_{TR}. Therefore, the actual image resolution degradation observed will be a blurring of a fraction, w, of the available signal in the ideal image by the PSF_{SS}, and the blurring of the remaining signal, $(1 - w)$, by the PSF_{TR}. A reasonable measure for quantitatively characterizing the combined blurring effects of the PSF_{SS} and PSF_{TR} is the average of the two FWHM weighted by the relative area of each function (Eq. (18))

$$FWHM_{avg} = FWHM_{SS} * w + FWHM_{TR} * (1 - w). \quad (18)$$

The effects of the SPSF, and consequently the PSF_{SS}, are determined by the sampling scheme and are unavoidable once the sampling choice is made. Therefore, the average FWHM has a lower bound of $FWHM_{SS}$. In the case of Spiral-SPRITE with a single spiral sampling scheme the $FWHM_{SS}$ is 1.6 pixels. To obtain high resolution images using a given sampling scheme the significance of PSF_{SS} must be maximized and PSF_{TR}

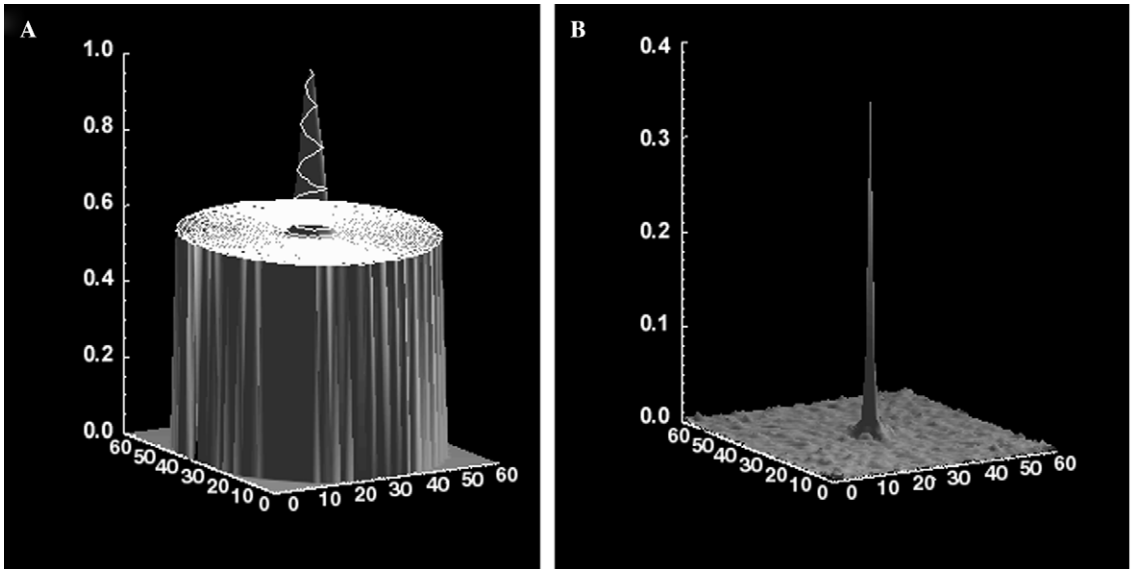

Fig. 5. (A) A shaded surface plot of the product, in k-space, of the sampling and longitudinal magnetization evolution functions for Spiral-SPRITE with a single spiral interleave sampling scheme. The spiral trajectory is traced out in white along the shaded surface plot. The x and y axes are k-space coordinates in pixels. The parameters used for this simulation were: $TR/T_1 = 2\%$ and $\alpha = 10°$. (B) A shaded surface plot of the Fourier transform of (A), i.e., the point spread function. The x and y axes are image space coordinates in pixels. This point spread function is comprised of a Lorentzian-like peak, which is slightly broadened at the base due to the evolution point spread function, and some low-lying structure at the extremities of image space due to omitted points in the k-space trajectory.

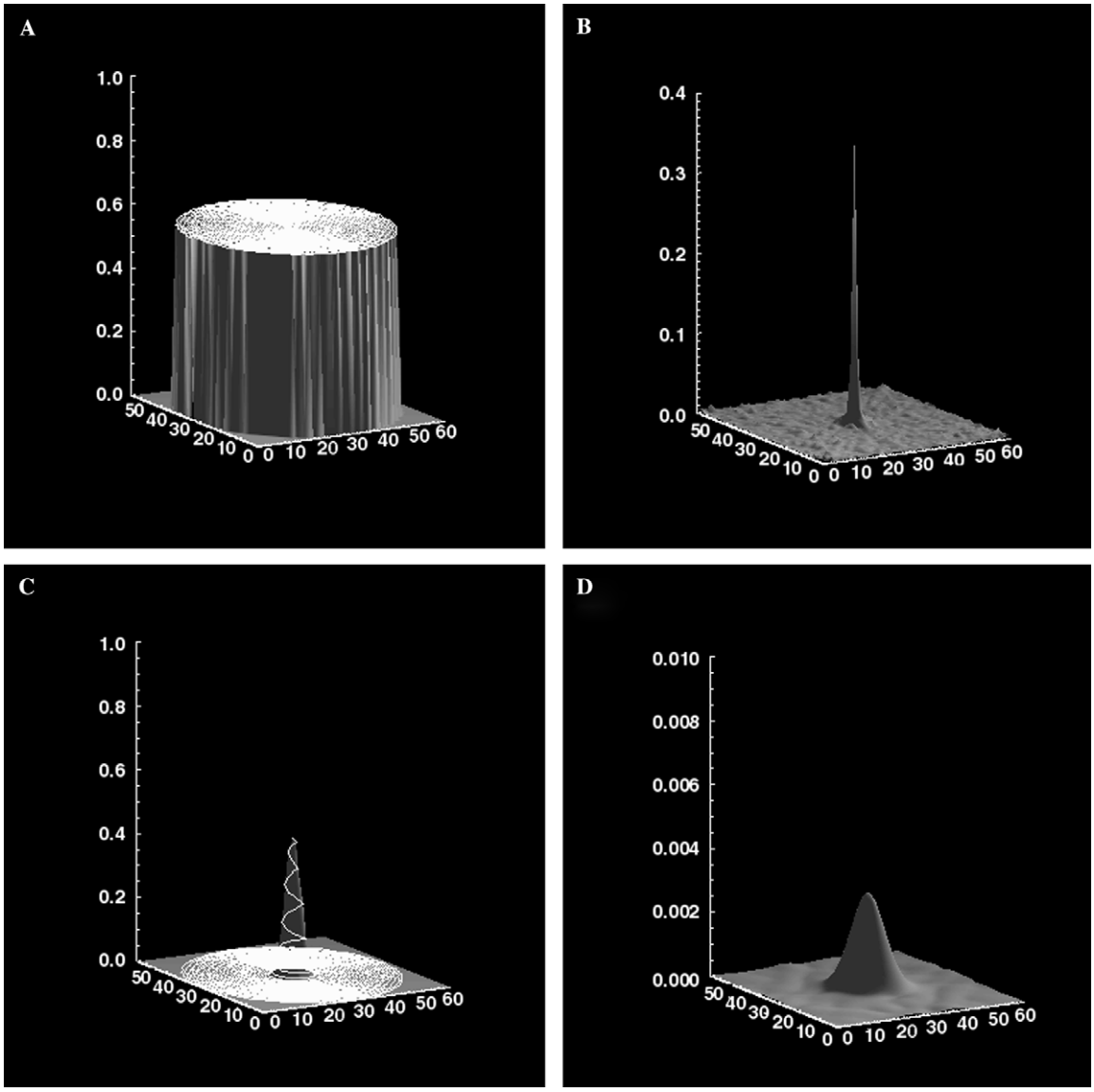

Fig. 6. (A) The steady-state portion of the k-space function depicted in Fig. 5A. (B) The Fourier transform of the steady-state function (PSF_{SS}). This function is the sampling point spread function with a relative area of w, the steady-state component (Eq. (16)). (C) The transient component of the k-space function depicted in Fig. 5A. (D) The Fourier transform of the transient function (PSF_{TR}). This function is representative of the effects of the evolution point spread function and has a relative area of $(1 - w)$. The linearity property of the Fourier transform ensures the sum of the point spread functions depicted in (B) and (D) is the PSF in Fig. 5B. Similarly the k-space functions in (A) and (C) sum to yield the k-space function in Fig. 5A.

minimized. From Eqs. (15)–(17) it is known that the relative significance of each constituent PSF and the width of PSF_{TR} are determined by the imaging parameters TR and α, but also by the sample dependent parameter, T_1. The imaging parameter, TR, affects image resolution but is also directly related to image acquisition time and the length of each phase encode gradient step. In practice this parameter is chosen with consideration given to acquisition time and duty cycle. The flip angle, α, is therefore the parameter which must be optimized. α appears in the signal equation and is also a resolution parameter. Hence, the optimal flip angle is the maximum value for α which can be employed without significant resolution degradation.

The Spiral-SPRITE k-space sampling trajectory can be implemented with any number, M, of interleaved spiral acquisitions. Increasing the number of spiral interleaves increases the experimental acquisition time because a delay must be introduced between each spiral trajectory to ensure full longitudinal magnetization recovery between spiral acquisitions. Offsetting this increase in acquisition time are the many advantages associated with spiral interleaves.

The introduction of spiral interleaves into the Spiral-SPRITE trajectory alters the form of the product of $U(t)$ and $R(t)$, in k-space. Fig. 5A depicts $U(t) * R(t)$ for a single spiral and Fig. 7A depicts $U(t) * R(t)$ for four interleaved spirals. Progressing out from the centre

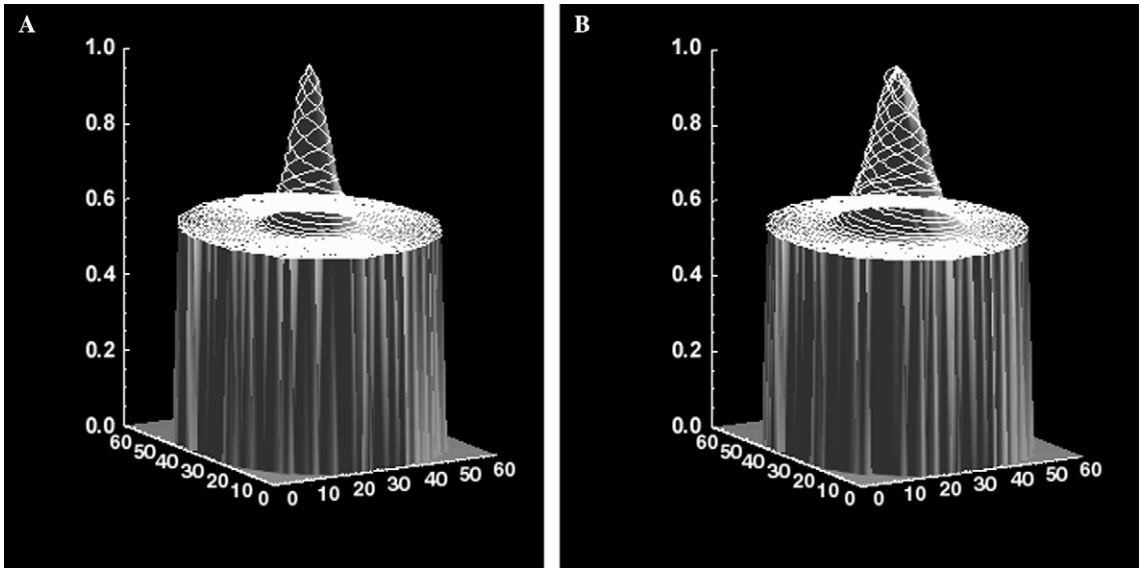

Fig. 7. (A) A shaded surface plot of the product, in k-space, of the sampling and longitudinal magnetization evolution functions for Spiral-SPRITE with four interleaved spirals. The spiral trajectory is traced out in white along the surface plot. The x and y axes are the k-space coordinates in pixels. Moving out from the centre of k-space, the signal decay to the steady state is demonstrably less rapid than that observed for the single spiral case (Fig. 5A). This effect becomes more prominent as the number of interleaves employed is increased, as demonstrated in (B) the eight interleaved spirals case. The simulation parameters used were the same as in Fig. 5: $\mathrm{TR}/T_1 = 2\%$ and $\alpha = 10°$.

of k-space, the effective exponential damping of the signal by this function is demonstrably much less rapid in the four spiral interleaves case than in the single spiral case. This effect becomes more significant as the number of interleaves is increased, as observed in the case of eight interleaved spirals, Fig. 7B. When transformed into image space, the transient portion of this function for the four spiral interleaves case results in a significantly narrower Lorentzian shape in the transient point spread function than that observed for the single spiral case. This suggests that the convolution blurring effect on actual image resolution becomes less significant as the number of spiral interleaves is increased.

Illustration of the 4D point spread functions, $\mathrm{FT}\{U(t) * R(t)\}$, associated with the 3D Conical-SPRITE k-space trajectory is problematic. Therefore, in this publication all point spread function developments are presented based on 2D Spiral-SPRITE experiments; however, the point spread function features described, and blurring characterization methods developed for the 2D case of Spiral-SPRITE are equally applicable to the 3D case of Conical-SPRITE.

3. Results/discussion

3.1. FOV scaling using the Chirp z-Transform

The images of the low water content hemp-polyester disc presented in Fig. 8 demonstrate the effective use of the Chirp z-Transform for FOV scaling. This algorithm has been developed and implemented in [12]. Figs. 8A and B present two images acquired within a multiple FID point acquisition with encoding times of 128 and 160 μs, respectively, reconstructed using a FFT. The SNR of these images was 6 and 4, respectively. The difference in FOV between these images is clearly evident. Figs. 8C and D show images reconstructed from the same FID points as in Figs. 8A and B, $t_\mathrm{p} = 128\,\mu\mathrm{s}$ and $t_\mathrm{p} = 160\,\mu\mathrm{s}$, respectively; however, in this case the CZT was employed for image reconstruction and FOV correction. The FOV correction employed was $Z = 0.8$ and $Z = 1.0$ for each image, respectively. The image SNR of Figs. 8C and D, was 6 and 4, respectively. Comparison between the images in Figs. 8B and D demonstrates the equivalency of image reconstruction with the FFT and CZT with $Z = 1.0$. Comparison between the images of Figs. 8A and C demonstrates the effectiveness of CZT for FOV scaling.

As expected, the SNR of the images in Figs. 8B and D are the same. The data set used for image reconstruction is the same in each case and the transforms used, the FFT and the CZT with $Z = 1.0$, are mathematically equivalent. The image in Fig. 8C was corrected to the same FOV as the images in Figs. 8B and D. The intensity was corrected such that the total intensity in the image remains unchanged over the FOV correction operation; however, the SNR of this image is significantly different to that of the images in Figs. 8B and D. The intensity correction was accomplished through the multiplication of the image intensity in each pixel, both that arising from signal and that arising from noise, by a

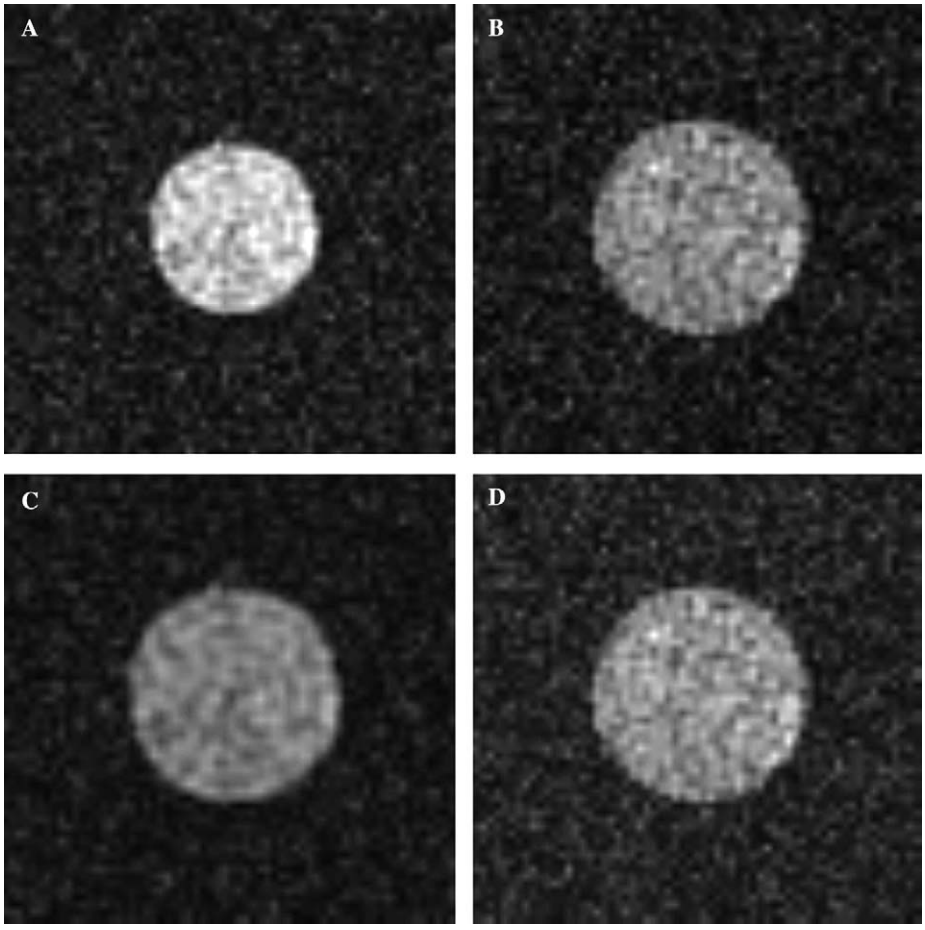

Fig. 8. 2D 64^2 single interleaf Spiral-SPRITE images of a low water content (3.7% by weight) hemp-polyester disc. Thirty-two FID points were collected over the range $t_p = 128$–$160\,\mu s$ with a dwell time of $1\,\mu s$. (A) 2D Spiral-SPRITE image reconstructed with a FFT from the FID point at $t_p = 128\,\mu s$ with FOV $= 10\,cm \times 10\,cm$ and SNR $= 6$. (B) 2D Spiral-SPRITE image reconstructed with a FFT from the FID point at $t_p = 160\,\mu s$ with FOV $= 8 \times 8\,cm$ and SNR $= 4$. (C) FOV-corrected 2D Spiral-SPRITE image reconstructed from the FID point acquired at $t_p = 128\,\mu s$. The Chirp z-Transform with $Z = 0.8$ was employed for image reconstruction yielding a FOV $= 8\,cm \times 8\,cm$ and SNR $= 6$. (D) 2D Spiral-SPRITE image reconstructed from the FID point with $t_p = 160\,\mu s$. The Chirp z-Transform with $Z = 1.0$ was employed for image reconstruction yielding a FOV $= 8\,cm \times 8\,cm$ and SNR $= 4$.

constant factor. Therefore, the SNR of the FOV corrected image (Fig. 8C) remains the same as the uncorrected image (Fig. 8A).

3.2. Signal averaging of multiple FID point images

The images of a low water content hemp-polyester disc shown in Fig. 9 demonstrate the SNR advantages of signal averaging multiple FID point images. Fig. 9A depicts an image reconstructed from a single FID point with $t_p = 160\,\mu s$. This image has an SNR of 4. Fig. 9B depicts an image reconstructed from the same single FID point, $t_p = 160\,\mu s$, but in this case the image was acquired with 9 console averages. This image has an SNR of 13. The images in Fig. 9A and Fig. 9B were acquired in 6 and 55 s, respectively. The gain in SNR by a factor of 3 required an increase in the acquisition time by a factor of 9.

Fig. 9C presents an image reconstructed from 9 FID points with an encoding time range of $t_p = 128$–$160\,\mu s$ and $\Delta t_p = 4\,\mu s$. The minimum FOV scaling factor employed was 0.8 and image SNR $= 18$. This image demonstrates a SNR improvement over the single FID point case in Fig. 9A by a factor of 4.5. This increase in SNR is gained without an increase in acquisition time. The increase in SNR between the 9 console averages case, Fig. 9B, and the 9 FID point averages case, Fig. 9C, is due to the SNR inconsistency effect associated with the intensity correction within the Chirp z-Transform FOV scaling algorithm.

Fig. 9D presents an image reconstructed from 16 FID points with an encoding time range of $t_p = 130$–$160\,\mu s$ and with $\Delta t_p = 2\,\mu s$. The minimum FOV scaling factor employed was $Z = 0.81$ and image SNR $= 18$. This image, reconstructed from the signal averaging of 16 FID point images, shows no additional SNR improvement

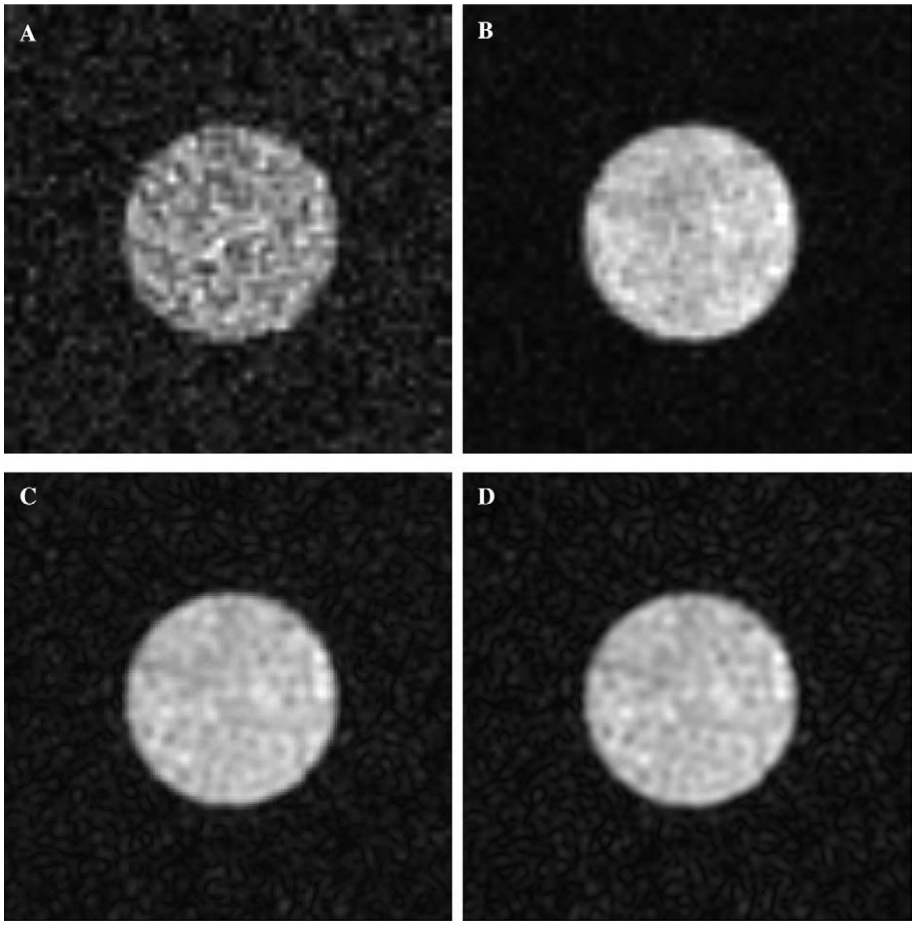

Fig. 9. 2D 64^2 single interleaf Spiral-SPRITE images of a low water content (3.7% by weight) hemp-polyester sample. Thirty-two multiple points were collected over the range $t_p = 128$–$160\,\mu s$. (A) 2D Spiral-SPRITE image reconstructed from the FID point at $t_p = 160\,\mu s$. This image was acquired in a single scan with an acquisition time of 6 s. SNR is 4. (B) 2D Spiral-SPRITE image reconstructed from the FID point a $t_p = 160\,\mu s$. This image was acquired in nine scans with an acquisition time of 55 s. SNR is 13. This SNR increase, a factor of approximately 3, is accompanied by an acquisition time increase of a factor of 9. (C) 2D Spiral-SPRITE image reconstructed from 9 multiple FID points in the single scan data set with a dwell time of 4 μs and an encoding time range of $t_p = 128$–$160\,\mu s$. The minimum FOV scaling factor employed was 0.8 and image SNR = 18. The gain in SNR, a factor of 4.5, is obtained with no acquisition time penalty. (D) 2D Spiral-SPRITE image reconstructed from 16 multiple FID points in the single scan data set with a dwell time of 2 μs and an encoding time range of $t_p = 130$–$160\,\mu s$. The minimum FOV scaling factor employed was 0.81 and image SNR = 18. No SNR improvement is observed beyond that of (C). The dwell time between multiple FID points violates the condition of noise correlation, Eq. (9), and the number of points is greater than the maximum given by Eq. (11).

than the image in Fig. 9C, where 9 FID point images are averaged. This is because the 16 FID point reconstruction violates the noise correlation condition (Eq. (9)). The filter width used in these experiments, 125 kHz, dictates that a minimum dwell time of 4 μs must be employed to obtain the maximum SNR advantage of multiple FID point averaging and Eq. (11) dictates that the maximum number of multiple FID point images which can be averaged for a SNR advantage, with $n = 64$ and $Z_{lim} = 0.8$, is 9. There were more multiple FID point images averaged for the reconstruction of the image in Fig. 9D, however, the number of multiple FID point images with uncorrelated noise which are averaged remains unchanged. Therefore, the observed SNR improvement over the single FID point case is the same in the case of both 9 and 16 FID point averages.

It would also be possible to enhance image SNR by processing the entire multiple FID point dataset using a regridding algorithm or an interpolation scheme, such as that developed by Dutt and Rokhlin [13]. It has been shown, however, that the Chirp z-Transform algorithm is capable of processing multiple FID point centric scan SPRITE datasets with greater accuracy, and in less time, than these interpolation methods [12]. The implementation and performance of this algorithm will be described in a forthcoming publication.

3.3. T_2^* mapping using multiple FID point images

Fig. 10A presents a T_2^* map of two $MnSO_4$ doped H_2O phantoms. Twenty FOV-corrected, multiple FID point ^1H Conical-SPRITE images, four from each of the

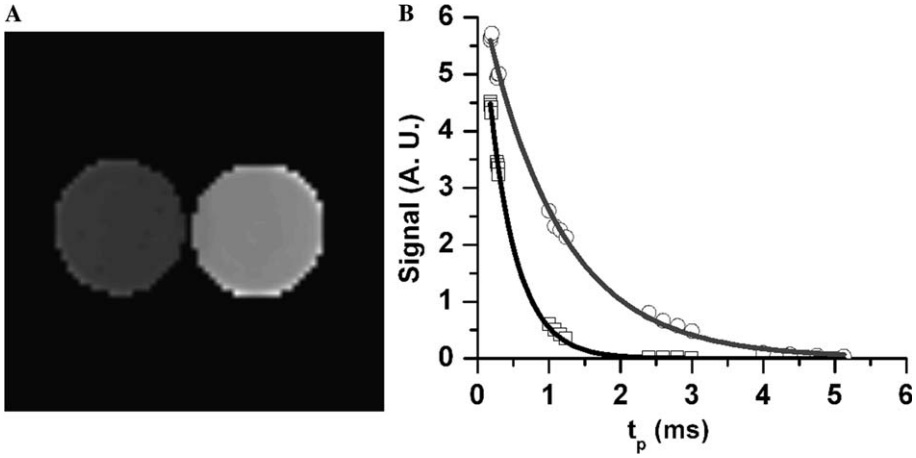

Fig. 10. (A) T_2^* map of two quasi-spherical $MnSO_4$ doped H_2O phantoms. The T_2^* map is highly homogeneous in the centre of each object. The inhomogeniety present at the edges of each sample arises from the resolution loss in the FOV scaling of the multiple FID point images. (B) Two representative T_2^* decays and the respective exponential fits from single voxels within the volume of each phantom. The single voxel T_2^* values, 1.07 ± 0.04 and 0.39 ± 0.01 ms, demonstrate reasonable agreement with the bulk values of 1.16 ± 0.01 and 0.41 ± 0.01 ms. The map was obtained from five multiple FID point Conical-SPRITE experiments in a total acquisition time of 64 min with two signal averages. Multiple point experiments were obtained with initial encoding times of: 180, 270 μs, 1.0, 2.4, and 4.0 ms, respectively, and with dwell times between each of the four multiple FID points of: 6, 10, 80, 200, and 375 μs, respectively. Each multiple FID point image was reconstructed using the Chirp z-Transform with $Z \geqslant 0.78$.

five independent acquisitions, were combined and a T_2^* decay defined for each voxel. Two representative single voxel T_2^* decays, one from within the volume of each doped water phantom, are presented in Fig. 10B along with the respective exponential fits. The single voxel T_2^* values of 1.07 ± 0.04 and 0.39 ± 0.01 ms demonstrate reasonable agreement with the bulk values of 1.16 ± 0.01 and 0.41 ± 0.01 ms, respectively. The T_2^* map is uniform in the centre of each object. The inhomogeneity present at the edges of each sample arises from the resolution loss associated with FOV scaling of the multiple FID point images.

According to Eq. (12), the T_2^* fit for each voxel provides a ^{1}H density value in addition to the T_2^* value. The ^{1}H density values obtained along with the T_2^* map in Fig. 10A were homogeneous across both samples. Therefore, the dependence of signal intensity on T_2^* is removed in a ^{1}H density map constructed from these values. The removal of T_2^* contrast is an important feature for many applications where true nuclei concentration values are desired. Such experiments include, for example, water content measurements of fluids in porous media applications and sodium content measurements in the brain for clinical applications.

3.4. Parameter optimization using point spread function simulations

The point spread functions for the 1, 4, and 8 interleaved spirals cases of Spiral-SPRITE and the 39 cones case of Conical-SPRITE were numerically simulated and the effect of varying the flip angle on the average FWHM (Eq. (18)) was explored. The rationale for using an average FWHM was outlined in Section 2.5. Fig. 11A is a plot of the $\mathrm{FWHM_{avg}}$ for each of the 1, 4, and 8 interleaved spirals and 39 cones sampling schemes as a function of flip angle, with a $\mathrm{TR}/T_1 = 1.3\%$. This TR/T_1 ratio is typical of polymer samples which are often characterized by a T_1 of hundreds of milliseconds. The horizontal reference line marks the lower bound of the $\mathrm{FWHM_{avg}}$, $\mathrm{FWHM_{SS}} = 1.6$ pixels. The vertical reference line represents the Ernst angle, given by

$$\cos\alpha = \mathrm{e}^{-\mathrm{TR}/T_1}. \tag{19}$$

This simulation suggests that the extent of blurring decreases as the number of spiral interleaves increases. Analogous simulations were obtained for the cases of $\mathrm{TR}/T_1 = 8.5\%$ (Fig. 11B) and $\mathrm{TR}/T_1 = 115\%$ (Fig. 11C). These simulations suggest that the optimal flip angle increases as TR/T_1 increases.

The results of the point spread function simulations were explored experimentally. The 2D 64^2 Spiral-SPRITE images in Fig. 12, acquired with a TR of 2 ms, feature three gelatinous water based samples corresponding to the TR/T_1 values simulated above: 1.3% (sample 1, top), 8.5% (sample 2, bottom-right), and 115% (sample 3, bottom-left). Fig. 12A presents a schematic of the samples, explicitly labeling the three TR/T_1 cases. The Spiral-SPRITE images in (B), (C), and (D) were acquired with 1 spiral, 4 interleaved spirals, and 8 interleaved spirals acquisition schemes, respectively. For the purposes of demonstrating blurring effects, the images presented were acquired with a large flip angle of 45°. The differences in intensity between samples within a single image arises from T_2^* contrast and differing sample volumes.

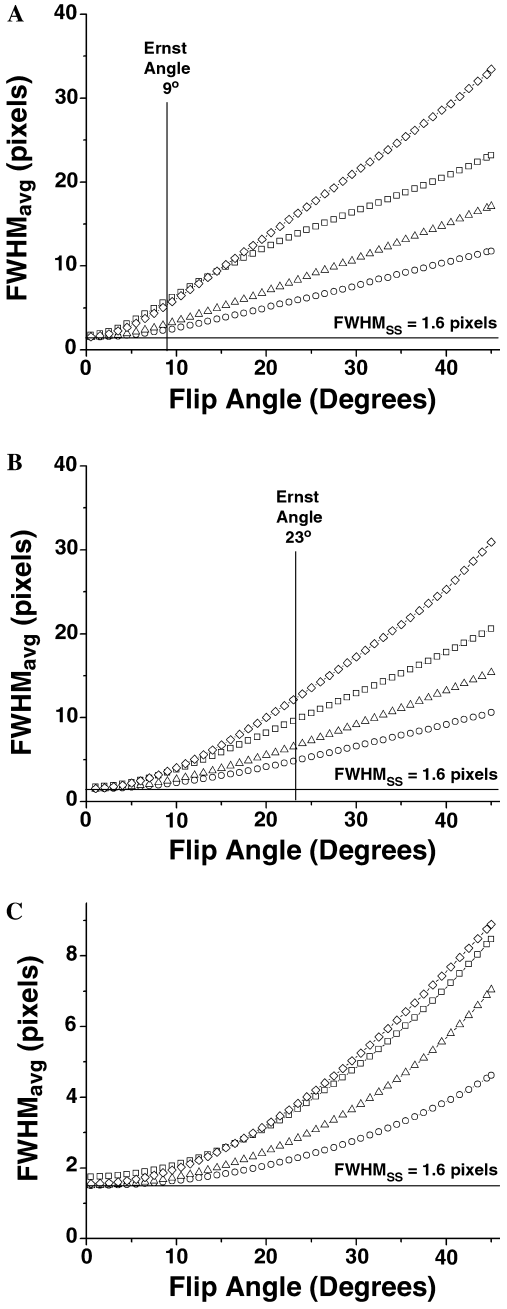

Fig. 11. The point spread functions for Conical-SPRITE with 39 conical trajectories and Spiral-SPRITE with 1, 4, and 8 interleaved spiral trajectories were numerically simulated over the range of flip angles from 0° to 45°. The weighted average FWHM (Eq. (18)) of the steady state and transient point spread functions as a function of flip angle are presented for the cases of (A) $TR/T_1 = 1.3\%$, (B) $TR/T_1 = 8.3\%$, and (C) $TR/T_1 = 115\%$. The horizontal reference line represents the lower bound of the average FWHM, $FWHM_{SS} = 1.6$ pixels. The vertical reference line in (A) and (B) is the Ernst angle. The (○), (△), (□), and (◇) symbols represent the 8 spirals, 4 spirals, 39 cones, and 1 spiral sampling schemes, respectively.

From Figs. 12B–D it can be seen that there is a significant reduction in blurring as the number of spiral interleaves increases. The difference in blurring of sample 1 ($TR/T_1 = 1.3\%$) and sample 2 ($TR/T_1 = 8.5\%$) in all three images of Fig. 12 demonstrates that blurring decreases as TR/T_1 increases. Sample 3 ($TR/T_1 = 115\%$) illustrates the limiting case of the relationship between TR/T_1, α, and blurring. When $TR/T_1 > 1$ the transient point spread function is so small with respect to the steady-state point spread function that even for large flip angles, 45° in this case, there is no significant blurring. Therefore, for the case of $TR/T_1 \geqslant 1$, blurring effects need not be considered when choosing α.

Fig. 13 presents x profiles taken through sample 1, at the point $y = 37$, in 2D images analogous to those presented in Fig. 12. The four profiles in each part of Fig. 13 correspond to images acquired with flip angles: 5.8°, 8.3°, 14.3°, and 20.8°, respectively. These profiles, for each of the (a) 1, (b) 4, and (c) 8 interleaved spirals sampling cases, illustrate the actual blurring observed over a range of flip angles for sample 1 ($TR/T_1 = 1.3\%$). It is interesting to note that the form of the blurring between the single spiral and the four and eight interleaved spirals cases is demonstrably different. In the single spirals case (Fig. 13A) the blurring forms a step-like function at the edges of the object, which becomes more pronounced as the flip angle increases. The blurring in the four and eight spirals cases (Figs. 13B and C) is more uniform, resulting in a rounding and broadening of the ideal boxcar profile.

In the case of the single spiral, the rapid exponential M_z decay from the centre of k-space, caused by the longitudinal magnetization evolution function, results in a transient point spread function, PSF_{TR}, which is significantly broader than the steady-state function. A fraction of the ideal image, a boxcar profile in this case, is blurred to a small extent by the steady-state function and the remaining signal intensity in the ideal image is burred significantly by the transient function. This results in a very broad boxcar superimposed on a slightly blurred boxcar. As flip angle increases, the significance of the transient point spread function, and therefore the amount of the ideal boxcar which is significantly blurred, increases and the step function-like blurring becomes more evident. This type of blurring is observed in Fig. 13A. In the four and eight interleaved spirals cases, the signal decay out from the centre of k-space is less rapid and therefore the width of the PSF_{TR} is much narrower than in the single spiral case. As a result, the extent of blurring due to the PSF_{SS} and PSF_{TR} are not as dissimilar as in the single spiral case and the blurring, as observed in Figs. 13B and C, appears more uniform.

It is clear from the profiles in Fig. 13 that there exists an optimal choice of flip angle. Consider the eight spirals case, Fig. 13C. A significant gain in signal intensity, with no significant loss to resolution, can be obtained through the choice of $\alpha = 14.2°$ over $\alpha = 8.5°$. Therefore, it is important to establish a guideline for determining the optimal flip angle for a given value of TR/T_1 and sampling scheme in order to maximize SNR.

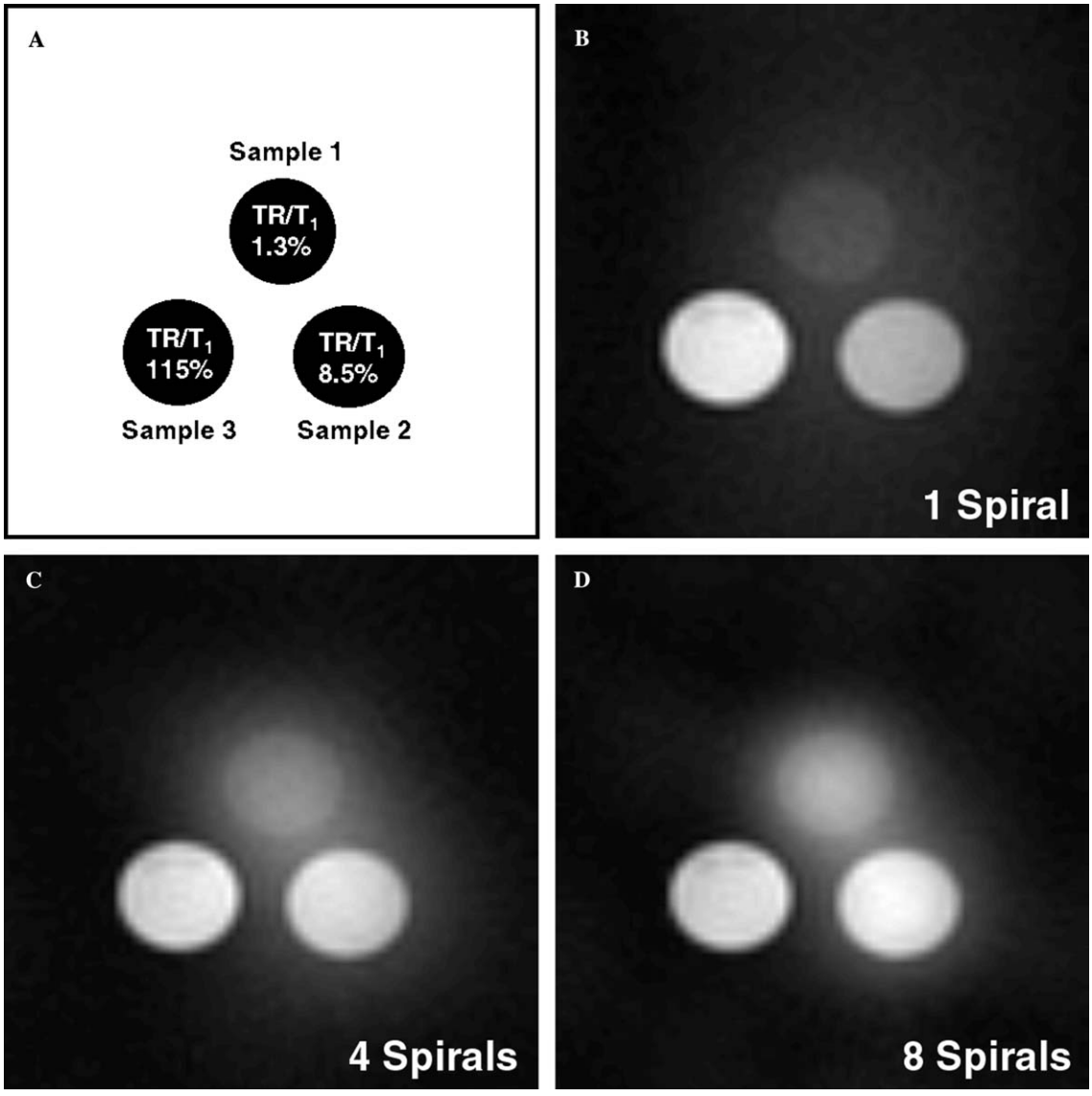

Fig. 12. 2D 64^2 Spiral-SPRITE images of three heavily doped water based gelatinous phantoms. Images were acquired with four scans with: $t_p = 150\,\mu s$, FOV $= 6 \times 6\,cm^2$, TR $= 2\,ms$ and flip angle $= 45°$. (A) A schematic of the three gelatinous phantoms. The TR/T_1 values for each sample were (1) 1.3% (top-centre), (2) 8.5% (bottom-right), and (3) 115% (bottom-left). The images presented were acquired with (B) 1 spiral, (C) 4 interleaved spirals, and (D) 8 interleaved spirals trajectories. These images demonstrate the relationship between blurring and the number of spiral interleaves and the value of TR/T_1. From the cases of $TR/T_1 = 1.3\%$ (sample 1) and $TR/T_1 = 8.5\%$ (sample 2), it is evident that the characteristic blurring is reduced as the number of interleaved spirals in the k-space trajectory is increased. Comparison between the blurring in the 1.3% case (sample 1) and the 8.5% case (sample 2) demonstrates that the blurring decreases as TR/T_1 increases. The case of $TR/T_1 = 115\%$ (sample 3) demonstrates the limiting case in which the evolutionary point spread function is insignificant with respect to the sampling point spread function and therefore even at a flip angle of 45°, no blurring of this sample is observed.

This can be achieved through comparison of the profiles in Fig. 13 and the PSF calculation at $TR/T_1 = 1.3\%$ in Fig. 11A. In the case of $\alpha = 5.8°$ the profiles show no evidence of significant blurring for any of the three sampling schemes. In the simulation, $FWHM_{avg} < 5$ pixels for all cases at $\alpha = 5.3°$. Significant blurring becomes evident in the profile for the single spirals case at $\alpha = 8.3°$, the four spirals case at $\alpha = 14.2°$ and the eight spirals case at $\alpha = 20.8°$. For the single spirals case, $FWHM_{avg}$ is greater than 5 pixels at $\alpha = 8.3°$. For the four spirals case, $FWHM_{avg}$ is less than 5 pixels at $\alpha = 8.3°$ but is greater than 5 pixels at $\alpha = 14.2°$. This trend is continued in the eight spirals case. The $FWHM_{avg}$ is less than 5 pixels at $\alpha = 8.3°$ and $\alpha = 14.2°$ but is greater then 5 pixels at $\alpha = 20.8°$. Therefore, a reasonable choice of optimal flip angle for a given sampling scheme can be obtained from the point spread function simulations by limiting the blurring parameter, $FWHM_{avg}$, to less than 5 pixels.

A point spread function simulation, limiting $FWHM_{avg} < 5$ pixels in order to determine the optimal flip angle, was performed for the 1, 4, and 8 spiral

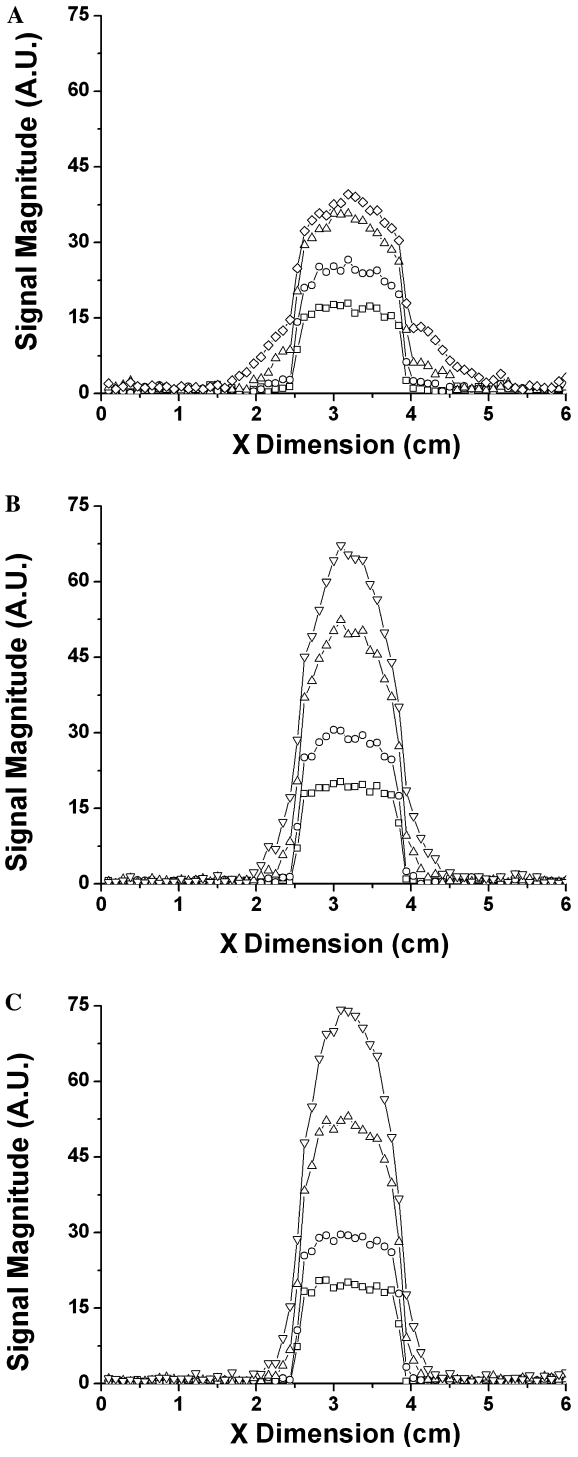

Fig. 13. X profiles through sample 1, $TR/T_1 = 1.3\%$ ($y = 37$), from 2D Spiral-SPRITE images analagous to those presented in Fig. 12. Profiles corresponding to the symbols (□), (○), (△), and (◇) are for flip angles, 5.8°, 8.3°, 14.3°, and 20.8°, in each of (A), (B), and (C). The *k*-space sampling schemes employed for image acquisition were (A) a single spiral interleaf trajectory, (B) a four interleaved spirals trajectory, (C) an eight interleaved spirals trajectory.

interleaves cases over a range of TR/T_1 values (0.5–30%). The results of these simulations are presented in Fig. 14. The lines on the graph correspond to the 1 spiral

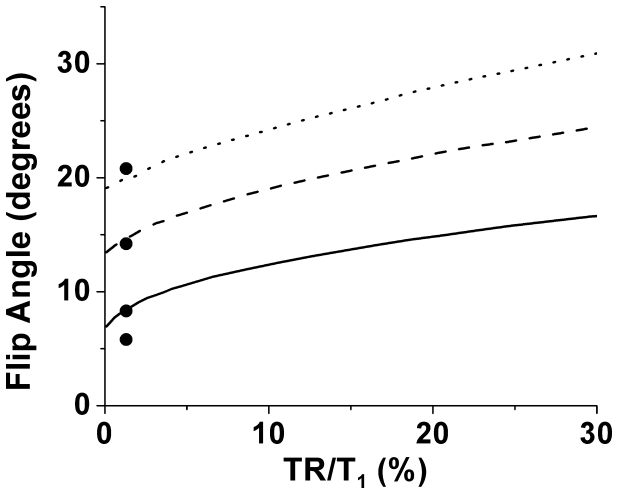

Fig. 14. The optimal flip angle for a range of TR/T_1 values (calculated from point spread function simulations with the limit $FWHM_{avg} < 5$ pixels) for the case of the 1 spiral (solid curve), 4 spirals (dashed curve), and 8 spirals (dotted curve) sampling schemes. The four profiles in each of Figs. 13A–C were acquired with parameters $TR/T_1 = 1.3\%$ and $\alpha = 5.8°$, 8.3°, 14.3°, and 20.8°, respectively. These parameters are marked with (●) on the graph. An image acquired with imaging parameters α and TR/T_1 corresponding to a point below the curve for a given sampling scheme has $FWHM_{avg} < 5$ pixels and therefore will not suffer from significant resolution degradation due to convolution blurring effects.

(solid line), 4 spirals (dashed line), and 8 spirals (dotted line) sampling cases. For any given value of TR/T_1 and choice of sampling scheme, images acquired with α values below the optimal flip angle line will have $FWHM_{avg} < 5$ pixels and therefore will not suffer from significant image degradation due to convolution blurring. The four points marked with (●) on the graph correspond to the parameters, $TR/T_1 = 1.3\%$ and $\alpha = 5.8°$, 8.3°, 14.3°, 20.8°, used in the four profiles shown in each of Fig. 13A–C.

Fig. 14 can be used to obtain optimal flip angles for the three Spiral-SPRITE sampling schemes. However, in the limiting case of $TR/T_1 \geqslant 1$ the blurring effects need not be considered when choosing a flip angle value and therefore the flip angle can be as large as other constraints (such as pulse duration and power deposition) allow.

The results presented in Fig. 14 can also be used to determine the optimal choice of sampling scheme. Consider the example of $TR/T_1 = 3\%$. The optimal flip angles are 9.6°, 15.9°, and 21.0° for each of the 1, 4, and 8 interleaved spirals sampling schemes, respectively. If we consider an experiment with M_z normalized to unity, the amount of signal excited using the optimal flip angle, $\sin\alpha$, will be 0.167, 0.274, and 0.358 for each sampling case respectively. The acquisition times are 23, 33, and 46 s, respectively. Therefore, we can calculate the sensitivity for each sampling scheme as

$$\text{Sensitivity} = \frac{\text{Signal}}{\sqrt{\text{Acquisition\_Time}}}. \quad (20)$$

Using Eq. (20), the sensitivities for the 1, 4, and 8 interleaved spirals cases are 0.035, 0.048, and 0.053, respectively. Therefore, for this experiment it can be concluded that the use of the 8 spiral interleaved sampling scheme with $\alpha = 21.0°$ will yield a high quality image with the maximum sensitivity.

4. Conclusions

Methods for producing rapid, high quality images and T_2^* maps of short signal lifetime systems using centric scan SPRITE methodologies were demonstrated. The efficiency of the centric scan SPRITE MRI techniques were optimized through the acquisition of multiple FID points following each RF excitation. Use of these FID points for signal averaging, SNR improvement, or for T_2^* mapping was demonstrated. The FOV correction necessary prior to recombination of the multiple FID point images for signal averaging or T_2^* mapping was achieved with the Chirp z-Transform algorithm. Numerical point spread function simulations were used to determine optimal k-space sampling schemes and imaging parameters for the centric scan SPRITE methods such that the SNR is maximized without significant resolution degradation due to point spread function convolution. The blurring resulting from the convolution of the ideal image with the point spread function was characterized by a weighted average of the full width half maxima values of the steady-state point spread function and the transient point spread function. A limit of 5 pixels for this characteristic blurring parameter was determined experimentally. Sampling scheme and flip angle choices with simulated point spread functions characterized by $\text{FWHM}_{\text{avg}} < 5$ pixels were demonstrated to result in images without significant resolution degradation.

5. Experimental

The Conical-SPRITE pulse sequence was implemented on an Oxford Magnet Technology (Oxford, UK) 4 T 925 mm i.d. horizontal bore superconducting magnet with a Siemens (Erlangen, DE) Sonata whole body gradient set (maximum gradient strength 4.0 G/cm). The console was a Varian (Palo Alto, CA) UnityInova. The RF probe was a 16 cm i.d., 16 element quadrature birdcage coil driven by a 7 kW pulsed amplifier (AMT).

In addition, the Conical-SPRITE and Spiral-SPRITE pulse sequences were implemented on a Nalorac (Martinex, CA) 2.4 T 32 cm i.d. horizontal bore superconducting magnet with a water cooled 7.5 cm i.d. gradient set (maximum gradient strength 100 G/cm) driven by Techron (Elkhart, IN) 8710 amplifiers. The RF probe was a ^{1}H free 32 element quadrature birdcage coil (Morris Instruments, Ottawa) driven by a 2 kW AMT (Brea, CA) 3445 RF amplifier. The console was a Tecmag (Houston, TX) Apollo. All experiments were performed at ambient temperature.

3D 64^3 multiple FID point Conical-SPRITE images were acquired, on the 4.0 T system, to demonstrate the use of multiple FID points for T_2^* mapping. The samples were two 180 ml quasi-spherical vessels containing water doped with $MnSO_4$. The first sample had a bulk T_2^* of 0.41 ± 0.01 ms and a bulk T_1 of 7.9 ± 0.1 ms. The second sample had a bulk T_2^* of 1.16 ± 0.01 ms a bulk T_1 of 24.5 ± 0.2 ms. The images were acquired in two averages with flip angle $= 6°$, TR $= 6.0$ ms, FOV $= 192$ mm $\times$ 192 mm $\times$ 192 mm and a delay between successive cones of 200 ms. Acquisition time for each experiment was 12 min and 46 s. Five multiple FID point experiments were obtained with initial encoding times of: 180, 270 μs, 1.0, 2.4, and 4.0 ms, respectively. Four FID points were acquired with Δt_p of 6, 10, 80, 200, and 375 μs in each experiment, respectively. The images from each multiple FID point were reconstructed using the Chirp z-Transform with $Z \geqslant 0.78$. These FOV-corrected images were combined and the T_2^* decay, defined for each voxel, was fit to a single exponential function using a Levenberg–Marquardt fitting procedure in IDL version 5.6 (Research Systems, Boulder, CO).

2D 64^2 multiple FID point Spiral-SPRITE images, employing a k-space trajectory with a single spiral interleaf, were acquired of a low water content sample, on the 2.4 T system, to demonstrate the use of multiple FID points for SNR improvement. The sample was a 4 cm diameter, 1 cm thick disc composed of a 100% hemp fiber mat in the commercial unsaturated polyester resin Stypol 040-8086 (Cook Composites). This sample had a water content of 3.7% by weight. The sample had a T_2^* of 1.0 ms and a T_1 of 64 ms. The images were acquired with flip angle $= 7.8°$, TR $= 2$ ms, FOV $= 8$ cm $\times$ 8 cm and a delay between successive spirals of 500 ms. Thirty-two multiple points were acquired with a dwell time of 1 μs following an initial encoding time, $t_p = 128$ μs. The optimal filter width of 125,000 Hz was used. The acquisition time for 1 and 9 scans were 6 and 55 s, respectively.

2D 64^2 Spiral-SPRITE images, employing k-space trajectories with 1, 4, and 8 spiral interleaves, were acquired of three short relaxation time gelatinous samples to explore the effect of the choice of sampling scheme and flip angle on image blurring. The first sample consisted of 60% sucrose, 5% gelatin, and 35% H_2O by weight. This sample had a T_1 of 23.4 ms and a T_2^* of 2.6 ms. The second sample was composed of 5% gelatin, 50% sucrose, 45% H_2O by weight and contained 80 mM $CuSO_4$. This sample had a T_1 of 154 ms and a T_2^* of 20 ms. The third sample contained 0.93% $MnSO_4$, 2% Agar, and 97% H_2O by weight.

This sample had a T_1 of 1.8 ms and a T_2^* of 190 μs. These Spiral-SPRITE images were acquired in four scans with FOV = 6 cm × 6 cm, t_p = 150 μs, TR = 2 ms and a delay between successive spirals of 800 ms. The acquisition times for the 1, 4, and 8 spiral interleave images were 23, 33, and 46 s, respectively.

SNR for all images was calculated as a ratio of the mean image intensity of a region of interest within the sample area compared to the mean image intensity from a similar region of the background.

Point spread functions were numerically simulated using IDL version 5.6 (Research Systems, Boulder, CO). The full width half maxima, for the Spiral-SPRITE cases, were calculated as the average diameter of the 2D half maximum contour of the simulated point spread function. In the 3D Conical-SPRITE case, the full width half maximum was calculated as the average diameter of the 3D surface representing the half maximum of the 4D point spread function.

Acknowledgments

B.J.B. thanks NSERC of Canada for operating and equipment grants. B.J.B. also thanks the Canada Chairs program for a Research Chair in MRI of Materials (2002-2009). M.H. thanks NSERC of Canada for a post-graduate scholarship, UNB for a John S. Little International Study Fellowship and Forschungszentrum Jülich for a travel grant. The UNB MRI Centre is supported by an NSERC Major Facilities Access grant. The 4T facility in Jülich is funded by the DFG (ZI 192/14-1) and the BMBF (01GO0104 and 01GO0204). We thank Michel F. Couturier, UNB Chemical Engineering for the hemp-polyester sample.

References

[1] B.J. Balcom, SPRITE imaging of short relaxation time nuclei, in: P. Blümler, B. Blümich, R. Botto, E. Fukushima (Eds.), Spatially Resolved Magnetic Resonance, Wiley-VCH, Toronto, 1998, pp. 75–86.

[2] C.B. Kennedy, B.J. Balcom, I.V. Mastikhin, Three-dimensional magnetic resonance imaging of rigid polymeric materials using single-point ramped imaging with T_1 enhancement (SPRITE), Can. J. Chem. 76 (1998) 1753–1765.

[3] S.D. Beyea, B.J. Balcom, P.J. Prado, A.R. Cross, C.B. Kennedy, R.L. Armstrong, T.W. Bremner, Relaxation time mapping of short T_2^* nuclei with single-point imaging methods, J. Magn. Reson. 135 (1998) 156–164.

[4] P.J. Prado, B.J. Balcom, I.V. Mastikhin, A.R. Cross, R.L. Armstrong, A. Logan, Magnetic resonance imaging of gases: a single-point ramped imaging with T_1 enhancement (SPRITE) study, J. Magn. Reson. 137 (1999) 324–332.

[5] S. Gravina, D.G. Cory, Sensitivity and resolution of constant-time imaging, J. Magn. Reson. A 104 (1994) 53–61.

[6] B.J. Balcom, R.P. MacGregor, S.D. Beyea, D.P. Green, R.L. Armstrong, T.W. Bremner, Single-Point ramped imaging with T_1 enhancement (SPRITE), J. Magn. Reson. A 123 (1996) 131–134.

[7] M. Halse, D.J. Goodyear, B. MacMillan, P. Szomolanyi, D. Matheson, B.J. Balcom, Centric Scan SPRITE magnetic resonance imaging, J. Magn. Reson. 165 (2003) 219–229.

[8] O. Heid, in: Sensitivity Enhanced Single Point Imaging, 6th Annual Meeting of the International Society of Magnetic Resonance in Medicine, 1998, p. 2186.

[9] L.R. Rabiner, R.W. Schafer, C.M. Rader, The Chirp z-Transform algorithm and its application, Bell System Tech. J. (1969) 1249–1292.

[10] M.C. Jeruchim, P. Balaban, K. Sam Shanmugan, Simulation of Communication Systems, Plenum Press, New York, NY, USA, 1992.

[11] I.V. Mastikhin, B.J. Balcom, P.J. Prado, C.B. Kennedy, SPRITE MRI with prepared magnetization and centric k-space sampling, J. Magn. Reson. 136 (1999) 159–168.

[12] J. Rioux, Non-uniform fast Fourier transformation of SPRITE MRI Data, B.CS. Thesis, University of New Brunswick, 2003.

[13] A. Dutt, V. Rokhlin, Fast fourier transforms for nonequispaced data, SIAM J. Scientific Comput. 14 (1993) 1368–1393.